EBioMedicine 54 (2020) 102740

Contents lists available at ScienceDirect

EBioMedicine

journal homepage: www.elsevier.com/locate/ebiom

# Bio responsive self-assembly of Au-miRNAs for targeted cancer theranostics

Weijuan Cai[a,b], Huan Feng[a], Liang Yin[b], Maonan Wang[a], Xuerui Jiang[a], Zhaojian Qin[a], Weiwei Liu[a], Chunmei Li[a], Hui Jiang[a], Yossi Weizmann[c,*], Xuemei Wang[a,*]

[a] State Key Laboratory of Bioelectronics (Chien-Shiung Wu Lab), School of Biological Science and Medical Engineering, Southeast University, Nanjing 210096, China
[b] Shunde Hospital of Southern Medical University, Shunde 528300, China
[c] Department of Chemistry, Ben-Gurion University of the Negev, Beer Sheva 8410501, Israel

ARTICLE INFO

*Article History:*
Received 24 January 2020
Revised 13 March 2020
Accepted 13 March 2020
Available online xxx

*Keywords:*
Nano-complexes
microRNA delivery
*In situ* self-assembly
Tumor microenvironment
Cancer treatment

ABSTRACT

*Background:* MicroRNA (miRNA) therapeutics are a promising approach to cancer treatment. However, this method faces considerable challenges to achieve tissue-specific, efficient, and safe delivery of miRNAs *in vivo*.
*Methods:* Herein, we developed a miRNA delivery system based on the *in situ* self-assembly of Au-miRNA nanocomplexes (Au-miRNA NCs). Within the cancer microenvironment, we constructed *in situ* self-assembled Au-miRNA NCs by coincubating gold salt and tumor suppressor mimics, such as let-7a, miRNA-34a, and miRNA-200a.
*Findings:* The *in vitro* experiments demonstrated that characteristic *in situ* self-assembled Au-miRNA NCs were present in cancer cells and can be taken up to inhibit the proliferation of cancer cells effectively. Most importantly, as proven in subcutaneous tumor treatment models, Au-miRNA NCs were especially useful for accurate target imaging and tumor suppression, with significantly enhanced antitumor effects for combination therapy.
*Interpretation:* These observations highlight that a new strategy for the *in situ* biosynthesis of Au-let-7a NCs, Au-miR-34a NCs, and Au-miR-200a NCs is feasible, and this may assist in the delivery of more miRNA to tumor cells for cancer treatment. This work opens up new opportunities for the development of miRNA tumor therapy strategies.
*Funding:* National Natural Science Foundation of China (91753106); Primary Research & Development Plan of Jiangsu Province (BE2019716); National Key Research and Development Program of China (2017YFA0205300).


## 1. Introduction

miRNAs are a class of endogenous regulatory noncoding RNAs found in eukaryotes that are approximately 20 to 25 nucleotides in length [1]. Mature miRNAs in the cytosol bind to the 3′-UTR region of target mRNA, repressing translation, and even directly degrading mRNA and inhibiting gene expression [2]. miRNAs modulate gene expression at the posttranscriptional level, while their aberrant expression in the circulation correlates with the most common human disorders, such as cancer. Numerous data have indicated that miRNAs are involved in tumorigenesis and tumor development [1–3]. In recent years, artificially synthesized miRNAs (amiRNAs) have been used to silence the expression of target genes and their functions. For example, chemically synthesized miRNA mimics can both specifically silence a single gene or simultaneously silence multiple related genes [4,5]. With the expansion of miRNA research in the field of tumors, the methods of miRNA-based antitumor treatment are likewise constantly evolving.

To date, studies have reported increased tumor cell chemosensitivity after introducing miRNA mimics, precompensating for missing miRNA functions, or inhibiting overexpressed miRNAs [2,6]. miRNA-based tumor therapy, especially synthetic mimics targeting tumorigenesis and metastasis, as well as cancer stem cell treatment or upregulation of specific miRNA levels to increase tumor chemosensitivity, can be a new strategy for treating cancer [7,8]. miRNAs that can function as tumor suppressors (*e.g.*, the let-7 family, miR-34a, and miR-200a) are underexpressed in many human cancers. In hepatocellular carcinoma, it has been shown that overexpression of different let-7 family members affects cell viability to varying degrees, especially let-7a has the greatest effect [9] miRNA mimics have been used in tumor therapeutic research, and some mimics have been approved for clinical trials [2,3,10]. Notably, a double-stranded let-7 mimic was shown to reduce migration and growth by inducing cell cycle arrest in lung cancer cell lines [6]. However, a series of severe problems, such as difficulty in being processed by cells, prolonged retention in tissues, easy degradation, and ineffective and unsafe delivery in the body, usually occurs after treatment by miRNA

* Corresponding authors.
*E-mail addresses:* yweizmann@bgu.ac.il (Y. Weizmann), xuewang@seu.edu.cn (X. Wang).

https://doi.org/10.1016/j.ebiom.2020.102740

**Research in context**

*Evidence before this study*

The success of miRNA therapeutics is highly dependent on the delivery of sufficient doses of miRNA to tumor cells. Gold nanoclusters (Au NCs) have excellent biocompatibility and can easily bind to certain target biomolecules.

*Added value of this study*

Using the specific microenvironment of cancer cells, we constructed *in situ* biosynthesis of Au-miRNA nano-complexes (Au-miRNA NCs). Through *in vitro* and *in vivo* experiments, our results indicate that a new strategy for *in situ* biosynthesis of Au-let-7a NCs, Au-miR-34a NCs and Au-miR-200a NCs are feasible, not only can miRNAs be delivered to target tumor cells or tissues, but also positively charged gold nanoclusters contribute to the immobilization of miRNAs, thereby exerting an inhibitory effect.

*Implications of all the available evidence*

Our data suggest that the original self-assembled Au-miRNA NCs can precisely target cancer cells. The combination of gene therapy and photo-thermotherapy (PTT) based on Au-miRNA NCs can achieve an improved anti-tumor effect. Therefore, the *in situ* self-assembled Au-miRNA NCs might be a valuable approach for effective and safe miRNA delivery.

mimic injection [1,11]. The pharmacokinetic properties of miRNAs also suggest that it will be challenging to achieve a sufficient concentration of miRNA in the tumor areas, which often results in limited effects of miRNA in the targeted tissue. Furthermore, abnormal tumor vasculature and high interstitial fluid pressure in the tumor microenvironment further inhibit miRNA delivery to the targeted tumor tissue [12,13].

Fortunately, nanotechnology has provided significant improvements in the delivery of molecules with low aqueous solubility, short circulation life, or unfavorable pharmacokinetics [14]. In fact, nanotechnology was utilized to overcome some of the limitations described above associated with the delivery of miRNAs [1]. As a new type of fluorescent nanomaterial, fluorescent metal nanoclusters have the advantages of easy preparation and modification, ultrasmall size, large Stokes shift, great biocompatibility, and adjustable fluorescence properties compared to traditional fluorescent dyes and quantum dots [15]. Therefore, these nanoclusters have a wide range of applications in biochemical analyses, environmental testing, medical imaging, and cancer treatment [16,17]. Metal nanoclusters usually exhibit a discontinuous energy level band state, and electrons can transition between energy levels and have properties different from those of metal nanoparticles with plasmon resonance features [18]. Among the most precious metal nanoclusters, gold nanoclusters (Au NCs) have excellent biocompatibility and can readily combine with targeted biomolecules. At present, tumor-targeted technology based on gold nanomaterials has been used extensively for noninvasive, quantitative, real-time, visual observation of life activities. The development of functionalized imaging probes with a high image-to-background ratio, good biocompatibility, and excellent optical properties is of great significance for locating cancer cells/tissues *in vivo*.

DNA and RNA are rich in various functional groups that bind to different metal ions. Therefore, they are ideal templates for synthesizing nanoclusters [19]. The position where the metal ion interacts with the nucleotide includes three possible sites, *i.e.*, the negatively charged oxygen atoms on phosphate groups, pyrimidines, and nitrogen atoms on the bases and hydroxyl groups on the deoxyribose units. Currently, increasing studies have indicated the interaction of metal clusters with DNA and RNA bases. Petty et al. determined that the relevant binding sites of metal nanoclusters are the $N_3$ atoms of cytosine [20], while another study indicated that guanine binds gold nanoparticles through nonbonding interactions [21].

On the basis of the above observations, we have developed a miRNA delivery system based on *in situ* self-assembled Au-miRNA nanocomplexes (Au-miRNA NCs), which exhibit biocompatibility, *in vitro* tumor targeting, fluorescence and enhanced Raman resonance imaging, as well as targeted antitumor therapy effects. Studies have shown that tumor cells/tissues spontaneously produce large amounts of oxidative substances (*e.g.*, reactive oxygen species, ROS; reactive nitrogen species, RNS; endogenous glutathione, GSH). Inflammatory diseases and tumor development are associated with the overexpression of these species [22]. This highly sensitive visualization of the relevant reducing substances and reactive oxygen species has clinical importance as a means of *in vivo* imaging [23]. Based on the observations that the tumor microenvironment has a completely distinct oxidative stress state, our study proposes a new strategy for using *in situ* self-assembled Au-miRNA NCs for targeted cancer cell imaging and treatment. Considering that tumor cells have a specific microenvironment that is entirely different from healthy cells [24–26], we induced the *in situ* self-assembly of Au with targeted miRNAs, including miR-34a, miR-200a, and let-7a, to achieve effective hepatocellular carcinoma (HCC) treatments [27–29]. In addition, gold nanoparticles have recently received much attention because of their unique physicochemical properties of nonviral gene delivery vectors, which have easy to modify surface functions [15,30]. It is already known that gold nanoparticles bind well to cytosine and guanine [20,21], which could further act as an effective carrier for miRNA delivery. Moreover, gold nanoparticles could act as photothermal agents for cancer treatment due to strong light absorption in specific areas, as shown in previous studies [31,32]. Therefore, the combination of gene therapy and photothermotherapy (PTT) based on Au-miRNA NCs could achieve improved antitumor effects.

Herein, we propose *in situ* self-assembled Au-miRNA NCs as a target miRNA delivery system with the remarkable advantages of avoiding high toxicity and transfection reagent and nanoparticle instability. It is worth mentioning that this simple approach not only solves the targeting and safety of miRNA drug delivery but also achieves sensitive multimodal imaging and tumor inhibition, in contrast to injecting fluorescent nanoparticles. Due to the unique tumor microenvironment, the self-assembled Au-miRNA NCs target only cancer cells; hence, they appear specifically in cancer cells and not in normal cells (*i.e.*, in human hepatocyte line L02).

## 2. Experimental section

### 2.1. Cell culture

HepG2, SMMC-7721 (human hepatocarcinoma) and HeLa cells were purchased from the ATCC (Manassas, VA). L02 cells (a human embryo liver cell line) were obtained from the Third Military Medical University (Chongqing, China). HepG2, SMMC-7721, L02 and HeLa cells were maintained in DMEM (high glucose, HyClone) supplemented with 10% fetal bovine serum (Gibco, Australia) and 1% penicillin/streptomycin (HyClone, Australia) at 37°C with 5% $CO_2$ in a 95% humidified atmosphere.

### 2.2. In situ *self-assembly of Au-miRNA NCs and relevant extraction*

When SMCC-7721 cells adhered, we added $HAuCl_4$ solution (Sigma Aldrich, USA; pH = 7.2; CAS: 16903-35-8) to the culture and ensured that the final concentration of the $HAuCl_4$ solution was 30 μM. Next, a miRNA mimic (dsRNA, 22 bp; Genepharma Shanghai, China) was added to the medium. After incubation of SMCC-7721 cells with

$HAuCl_4$ solution and miRNA mimic for 24 h or 48 h, the medium was discarded. Then, the cells were washed with PBS 2-3 times and trypsinized for 1 min; the residual trypsin solution was removed, 2 mL PBS was added, and the samples were centrifuged at 1500 rpm for 3 min. The supernatants were discarded, and the cells were resuspended with deionized water. Using the repeated freeze-thaw method, the cells were placed in liquid nitrogen for 5 min and immediately transferred to a 37 °C water bath for 10 min. Such cycles were repeated 3−4 times until the cells were completely lysed. The cell lysates were further centrifuged at 2,500 rpm for 20 min, and the supernatants were removed by filtration through a 0.22 μm filter to obtain cell extracts for further characterization. The concentrations of miR-34a, miR-200a and let-7a were 100 nM, 50 nM and 100 nM, respectively. The concentration of the gold salt ($HAuCl_4$ solution) in SMMC-7721 cells was 30 μM.

### 2.3. Optical properties of the in situ self-assembled Au-miRNA NCs

The UV−Vis absorption and fluorescence spectra were measured using a UV−Vis−NIR spectrophotometer (Thermo Scientific Evolution 260, USA) and a fluorescence spectrometer (RF-5301PC, Japan), respectively. SMMC-7721 cell extracts were deposited on the flat back of aluminum foil and used for surface-enhanced Raman scattering (SERS) (Renishaw, UK) studies by stimulation with a laser at 785 nm. Infrared absorbance detection was performed using a Fourier transform infrared (FTIR) spectrometer (Thermo Scientific Nicolet iS5, USA). Each sample was repeated three times.

### 2.4. Transmission electron microscope (TEM)

The Au-miRNA NC extracts were diluted with deionized water, dropped onto a copper mesh, and dried naturally. A JEM-2100 TEM was used to characterize the size and size distribution of the *in situ* biosynthesized Au-miRNA NCs.

### 2.5. Atomic force microscope (AFM)

An AFM (Bruker Dimension Icon, USA) was used to study the morphology of Au-miRNA NCs. A high-speed precision XYZ closed-loop scanning tube was used to isolate 85 dBC of continuous noise in the environment. The microscope optical system contained a 5-megapixel digital camera. A highly doped single-crystal silicon tip (tip radius ~10 nm) with a measurement accuracy of 0.1 nm was used. During sample preparation, the mica flakes were soaked in $Mg^{2+}$ solution for 5 min in advance, and the samples were then diluted with deionized water and dropped on the mica plate, left to stand for 5 min, gently washed with distilled water and dried with $N_2$. To verify the presence of miRNA in Au-miRNA NCs, digestion was performed using Rnase A (Biofroxx, Germany) and 30 min later in the same region for AFM detection.

### 2.6. Fluorescence confocal microscope

Nanocluster imaging of cultured media: A total of $1 \times 10^6$ cells were plated onto a laser confocal Petri dish (801002, Houbai Nanjing). After 12 h or 24 h of incubation, a confocal microscope with a 488 nm laser was used for imaging the samples, and emission was measured at 670 nm. Nanocluster imaging of cell extracts: After 24 h or 48 h incubation with $HAuCl_4$ and miRNA, we harvested the cells and obtained cytoplasmic extracts. The presence of biosynthesized Au-miRNA NCs was characterized by fluorescence confocal microscopy using a 488-nm excitation laser beam (Andor Revolution XD) and a 203 IR coated objective (Nikon Eclipse C1, Japan). Each sample was repeated three times.

### 2.7. Scratch assays

Scratch assays were performed with SMMC-7721 cells and HepG2 cells coincubated with $HAuCl_4$ and miRNA, and a thin wound was introduced by scratching with a pipette tip. Then, at 0 h, 12 h, 24 h and 36 h post-scratching, cell images were obtained and analyzed by Image J software. In SMMC-7721 cells, the concentrations of miR-34a, miR-200a and let-7a were 100 nM, 50 nM and 100 nM, respectively, and the concentration of the gold salt was 30 μM. In HepG2 cells, the concentrations of miR-34a, miR-200a and let-7a were all 50 nM, and the concentration of the gold salt was 5 μM.

### 2.8. Cytotoxicity assessment and cytostatic test

Cell viability was measured by 3-(4,5-dimethylthiazol-2-yl)-2,5-diphenyltetrazolium bromide (MTT) assays. First, $HAuCl_4$ (pH = 7.2) was diluted with PBS to create a corresponding concentration solution. Toxicity tests for the *in situ* synthesis of Au NCs were performed. HepG2, SMMC-7721 and L02 cells in logarithmic growth phase were trypsinized and then seeded in 96-well plates (4,000 cells per well were inoculated with 200 μL complete cell medium). After 24 h of resting time, each cell type was rinsed with DMEM and incubated with various concentrations of $HAuCl_4$ solutions (0.5, 1, 5, 10, 30, 50, 100, 200, 500, and 1000 μM) for 48 h. MTT solution was then added, and the cells were further incubated for 4 h. DMSO was added to solubilize the formazan crystals, and OD at 490 nm was recorded. The appropriate concentration of $HAuCl_4$ in different cell lines was then determined. Next, the miRNA mimic was diluted with ultrapure DEPC $H_2O$ to the indicated concentration (10, 50, 100, 200, 500, and 1000 nM) to determine the optimal miRNA concentration. The subsequent steps were the same as those detailed above. Finally, for the cytostatic test, HepG2 and SMMC-7721 cells in the logarithmic growth phase were prepared and seeded in 96-well plates in a single cell suspension. After 24 h of resting time, each cell type was rinsed with DMEM and incubated with miRNA and $HAuCl_4$ and then incubated for 0 d, 1 d, 2 d, 3 d, 4 d, and 5 d. The cell growth curve was plotted at each time point. Three biological replicates per experiment were used. For the cytostatic test in SMMC-7721 cells, the concentrations of miR-34a, miR-200a and let-7a were 100 nM, 50 nM and 100 nM, respectively, and the concentration of the gold salt was 30 μM. In HepG2 cells, the concentrations of miR-34a, miR-200a and let-7a were all 50 nM, and the concentration of the gold salt was 5 μM.

### 2.9. Total RNA extraction and real-time quantitative PCR (qRT-PCR)

In brief, total RNA was extracted from cells using a TRIZOL kit (Tiangen, China). Then, cDNA was synthesized from 100 ng of total RNA using RevertAid Reverse Transcriptase (Fermentas, Canada) for the following miRNA qRT-PCR analysis. qRT-PCR for miR-34a, miR-200a and let-7a was performed with a SYBR Green PCR kit (Shanghai Jima Co., Ltd.) in accordance with the manufacturer's instructions, with U6 as an internal reference. The qRT-PCR samples were preincubated for 5 min at 95°C, followed by 40 cycles of denaturation for 12 s at 95°C and annealing for 40 s at 62°C. Reactions containing neither reverse transcriptase nor template served as negative controls. PCR amplification was carried out on an Applied Biosystems step one Plus Real-Time PCR instrument. Each sample was repeatedly measured three times, and the relative expression of the gene was analyzed by the $2^{-\Delta\Delta CT}$ method. The miRNA was subjected to the stem-loop method. The specific primer sequences are listed in Table S1.

### 2.10. Western blot analysis

Cell lysis and protein sample collection were performed on ice. An appropriate amount of protein loading buffer was added to the collected protein samples and heated in a boiling water bath at 100 °C for

3 to 5 min to completely denature the proteins. SDS-PAGE electrophoresis was performed using a 10% separation gel and a 5% concentrated gel, and PVDF membrane transfer was performed by the electrotransfer method. The membrane was blocked with a 5% blocking solution for 1 h at room temperature, and an anti-c-myc primary antibody (1:500) was added at 4 °C overnight; then, TBST was used to wash the membrane 3 times for 15 min each time, and an HRP-labeled secondary antibody was added (1:1000) for 2 h. Finally, after incubation with developer solution, the blot was captured on a Bio-Rad chemiluminescence imager. Optical density value (A) analysis was performed using Quantity One software, and GAPDH was used as an internal control. The optical density ratio of the target protein to GAPDH was calculated. This experiment was replicated three times.

### 2.11. Luciferase reporter assay

The 3'-UTR fragment of c-myc containing the let-7a binding sequences containing c-myc putative binding sites was constructed into the pmirGLO dual luciferase reporter vector. A mutated plasmid was used as a control (Genepharma Shanghai, China). All constructs were verified by DNA sequencing. HeLa cells were plated in 24-well plates and then cotransfected with 50 ng of constructs with or without the let-7a mimic (30 nM). At 48 hours after transfection, luciferase activity was detected using a dual-luciferase reporter assay system (Promega, Madison, WI, USA) according to the manufacturer's instructions and normalized to Renilla activity. Three sets of repetitions per group were performed.

### 2.12. Experiments of mirror-loaded cell culture microcavity

The experiments of mirror-loaded cell culture microcavity were based on a mini cell culture device designed by our research group (Patent CN201811228087.2). This microcell culture device can be used with microscopes and other experimental platforms. At the same time, it uses sensing and PID control technology to precisely control the temperature and humidity in the microcavity. And $CO_2$ concentration can provide cells with an incubation environment suitable for cell growth, which can efficiently and stably maintain the required external environment to ensure the cell's proliferation and vitality. In this study, SMMC-7721 cells were linked with let-7a and $HAuCl_4$ solution for 6 h and then transferred to a mirror-loaded cell culture microcavity. We traced the temporospatial processes of cell division blockade and cell death by fluorescent Au-miRNA NCs. Photographed using a confocal microscope with an excitation wavelength of 488 nm at 0 h, 0.5 h, 1 h, 2 h, 3 h, 4 h, 5 h, and 6 h.

### 2.13. The effect of Au-miRNA NCs on cell apoptosis

SMMC-7721 cells ($1 \times 10^5$ cells/well) were incubated with $HAuCl_4$ (30 μM) and let-7a (100 nM) for 6 h in confocal dishes. In the laser irradiation group, the cells were exposed to a 640 nm laser for 8 min, while in the control group, the cells were not subjected to laser irradiation. After 24 h of incubation, single cell suspensions were collected in 1.5 mL EP tubes. The cells were mixed thoroughly with 5 μL of Annexin V-FITC in 500 μL of dispersion binding buffer and then stained in the dark for 15 min at room temperature. Next, 5 μL of PI was added to the stained cells, and the mixture was kept in the dark for 5 min. The apoptotic rates were detected using a flow cytometer and use Flowjo software for analysis.

### 2.14. Construction of the xenograft tumor mouse model

Three-week-old BALB/c athymic nude mice were purchased from Peking University Health Science Center. All animals were maintained in a specific pathogen-free (SPF) environment at approximately 25 °C with a standard 12 h light/12 h dark cycle. The animals were allowed free access to tap water and food in the form of a standard pellet diet. Tumor xenograft models were generated by the subcutaneous inoculation (100 μL volume containing $5 \times 10^7$ cells/mL media) of HepG2 cells in the right/left side of their abdomen using a 1-mL syringe with a 25 G needle.

### 2.15. Therapeutics for the tumor mouse model

For the *in vivo* treatment assays, we established HepG2 subcutaneous tumors in 4∼5-week-old BALB/c nude mice (n = 4−5). The tumors were allowed to grow for approximately 1 week to reach a volume of 30−40 $mm^3$. Subsequently, PBS (control), Au NCs (2 mM $HAuCl_4$, 100 μL), let-7a (2 μM, 100 μL), and Au-let-7a NCs (2 mM $HAuCl_4$, 100 μL; 2 μM let-7a, 100 μL) were injected subcutaneously in the vicinity of the tumor sites in different groups, followed by *in vivo* fluorescence imaging at 0 h, 2 h, 12 h, 24 h and 48 h (excitation filter of 460 nm). The mice were placed under anesthesia using 2% isoflurane gas, and the experimental results were recorded with an Optical Imaging System for Small Animals (Perkin Elmer, IVIS Lumina XRMS Series III) according to the manufacturer's instructions.

The HepG2 tumor model was successfully constructed, and the mice were injected subcutaneously with PBS, $HAuCl_4$, let-7a, and $HAuCl_4$ and let-7a solutions on days 0, 3, 6, 9, 12 and 15 (n = 4-5 mice per group). On day 18, we euthanized all mice and harvested the tumor xenografts for further analyses.

In addition, we established HepG2 subcutaneous tumors in 4∼5-week-old BALB/c nude mice (n = 3) and allowed the tumors to grow to a volume of 100 $mm^3$. PTT treatment (808 nm, 10 min, 1 W) was performed 12 h after injection of only gold salt, PBS, or biosynthesized Au-let-7a NCs. All experiments involving mice were approved by the National Institute of Biological Science and Animal Care Research Advisory Committee of Southeast University, and the experiments were conducted following the guidelines of the Animal Research Ethics Board of Southeast University.

### 2.16. Hematoxylin and eosin (H&E) staining

Sections of the major tissues, including the heart, lungs, liver, spleen, kidneys and tumors, were fixed in 10% formaldehyde, dehydrated, and paraffin-embedded. The sections were stained with hematoxylin for 1 min and eosin for 7 min.

### 2.17. Reagent introduction

All other commercially obtained chemicals were of analytical grade. Purified water was used after deionization and filtration in a home supplied Millipore system.

### 2.18. Statistical analysis

All the experiments were carried out in triplicate. Quantitative values are expressed as mean ± standard deviation (SD), statistical analyses were performed using Student's *t* test. Two-way ANOVA was used for paired observations and repeated measures over time. Statistical significance was set at $P < 0.05$ (two-tailed). The statistical analyses were done with GraphPad Prism software (Version 5.01, GraphPad, San Diego, CA, USA) and SPSS for Windows version 19.0 (SPSS Inc, Chicago, IL, USA).

## 3. Results and discussion

### 3.1. In situ *self-assembly of Au-miRNA NCs*

The main goal of this work was to realize the *in situ* self-assembly of Au-miRNA NCs with high cancer cell/tissue-targeting capability for bioimaging and theranostics (Fig. 1). It is well known that the tumor

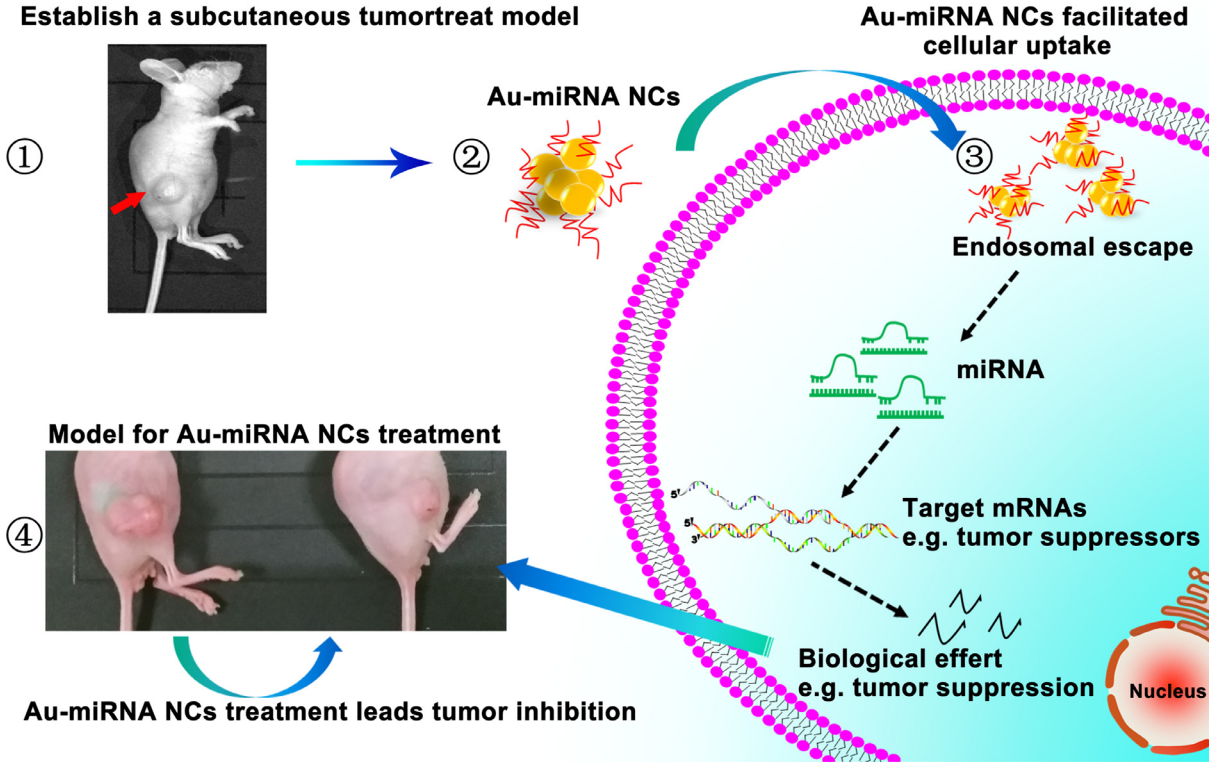


**Fig. 1.** Schematic illustration of *in situ* self-assembled Au-miRNA NCs for cancer inhibition.

microenvironment is different from that of normal tissue due to different pH values and elevated concentrations of ROS, RNS, and GSH, etc. [33,34]. The excess reductant substances in cancer cells can readily facilitate to reduce metal ions such as Au (III) in $HAuCl_4$ to biosynthesize fluorescent Au nanoclusters (Au NCs) [35]. The relevant bases of miRNA mimics were negatively charged [36]. Therefore, the *in situ* self-assembled fluorescent Au-miRNA NCs can readily occur within the specific microenvironment of cancer cells, which can be further utilized for accurate diagnosis and precise treatment of malignant tumors. The principle is to take advantage of the classical mechanism of the biomineralization of inorganic ions involved in the reduction and sequent complexation of miRNAs. Au (III) salt reduction can co-occur during miRNA interaction and efficient miRNA intracellular transfection to construct *in situ* self-assembled Au-miRNA NCs [37,38]. HepG2 and SMMC-7721 cells and the human hepatocyte cell line L02 were utilized as experimental models to evaluate the feasibility of this strategy for individual cells and tumors (Fig. S1).

To confirm the formation of Au-miRNA NCs, we further explored laser confocal fluorescence imaging of target cancer cells with *in situ* self-assembled Au-miRNA NCs. In this study, HepG2 and SMMC-7721 cells were initially incubated with $HAuCl_4$ solution and miR-34a/miR-200a/let-7a for 24 h. We found that both HepG2 and SMMC-7721 cells can spontaneously form fluorescent gold nanoclusters, and the *in situ* self-assembled Au-miRNA NCs were well dispersed in the cells around their nucleoli, which outlined the cell contours in fluorescence imaging (Fig. 2a). In addition, the groups cultured with Au-miRNA NCs showed much stronger intracellular fluorescence than the groups cultured with only the $HAuCl_4$, while the L02 cells did not have intracellular fluorescence under all experimental conditions.

Based on these observations, we further harvested the cells and obtained cytoplasmic extracts. Initially, we used TEM, AFM, confocal microscope tracking imaging, and other methods to characterize the targeted delivery of Au-miRNA NCs in hepatocellular carcinoma. The typical TEM images of the SMMC-7721 cell lysate clearly illustrated the *in situ* self-assembled Au-miRNA NCs. Gold nanoclusters with diameters of approximately 2 nm were clearly visible in the presence of miR-34a, miR-200a, and let-7a (Fig. 2b–d). This is consistent with the results observed in our previous studies [37]. Obviously, Au-miRNA NC polymers varied in size among these groups. Larger polymer aggregation occurred in the miR-34a group, and the let-7a group had small aggregation with a relatively uniform diameter. To explore the morphology of the Au-miRNA NCs, we performed AFM visualization of SMMC-7721 cell lysates. The Au-miR-34a NCs group, with a typical larger aggregation observed under TEM, was characterized by AFM at the same time. It was evident that miRNA was readily be adsorbed on gold nanoclusters, and a large amount of Au-miRNA NCs aggregated to form a regular nanostructure (Fig. 2e). To demonstrate the specific role of miRNAs, the extracted polymer nanostructures were subjected to Rnase A digestion. After 30 min, significantly reduced aggregation was observed in the same region (Fig. 2f and g). After digestion, the dispersed Au-miRNA polymeric NCs were clearly visible. Similar topography could also be observed from AFM images of the *in situ* self-assembled Au-miRNA NCs in the presence of miR-200a and let-7a, as illustrated in Fig. S2a and b. From the vertical coordinates of the AFM topography (bottom panel, Fig. 2e–g), it is evident that the cumulative height of the Au-miRNA NCs was ca. 4 nm, while the size of the relevant RNA double helices is estimated to be ca. ~2 nm. In comparison, a typical AFM image of the SMMC-7721 cells cultured with only $HAuCl_4$ solution indicates that the greatest size of the sample is only 1.6 nm, and we can only see one substance (Au) in the phase diagram (Fig. S3a). This observation is consistent with the characterization by TEM. In addition, when using only miRNA as a control under the same experimental conditions, *i.e.*, SMMC-7721 cells cultured with the corresponding miRNA alone, no Au-miRNA NCs were found (Fig. S3c-e). It is worth mentioning that under identical experimental conditions when miRNA and $HAuCl_4$ solution were simultaneously added to L02 cells, no Au-miRNA NCs were observed (Fig. S3b). This indicates that the tumor microenvironment is essential for the *in situ* self-assembly processes.

It is evident that both purine and pyrimidine bases have a conjugated double bond and are the main chromophore in RNA, which is capable of absorbing ultraviolet radiation between 200 and 300 nm

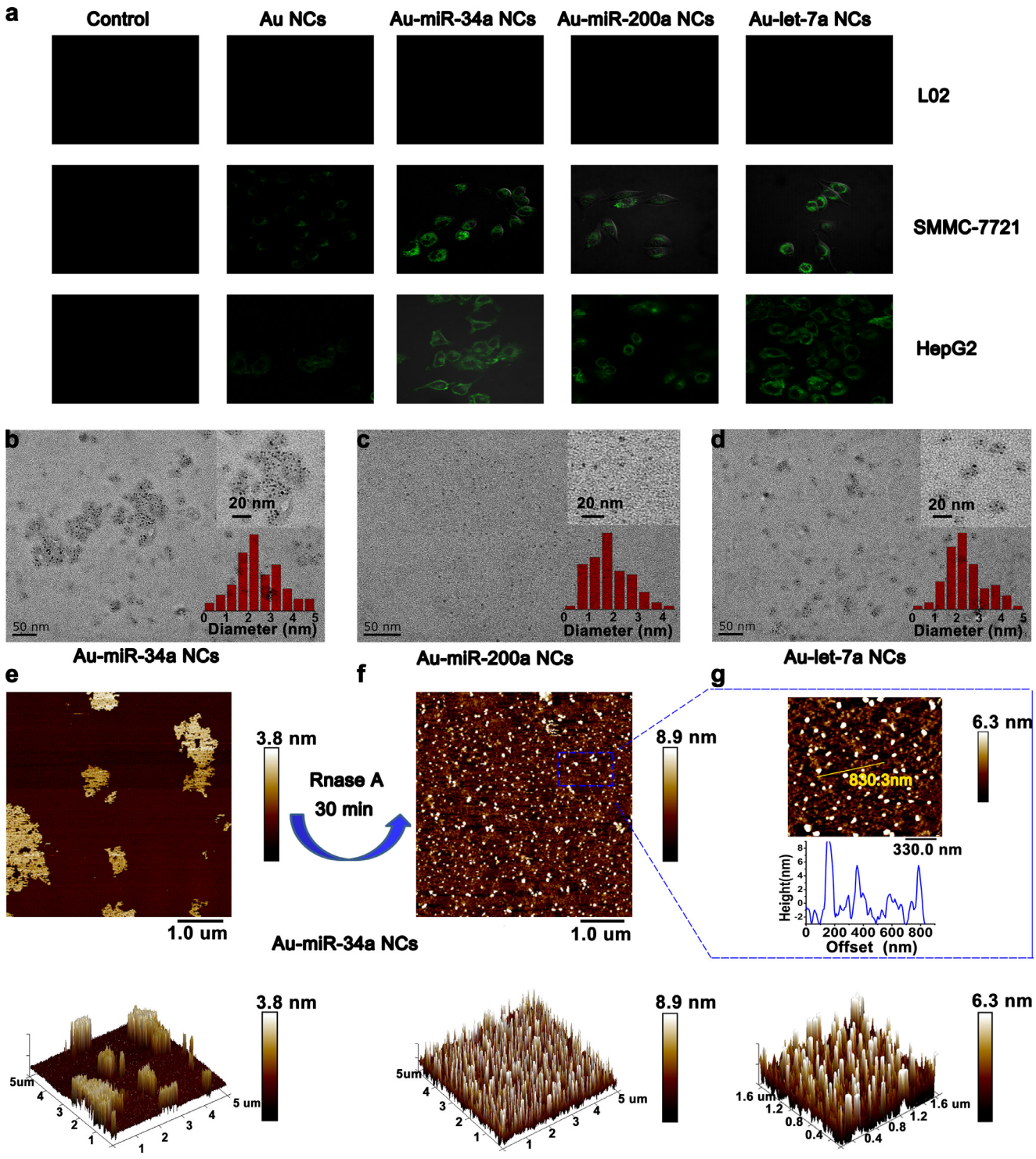


**Fig. 2.** Physicochemical properties of *in situ* synthesized fluorescent Au-miRNA NCs. (a) Visualization of Au-miRNA NCs in SMMC-7721 (hepatoma cell line), HepG2 (hepatoma cell line), and L02 (normal hepatocyte cell line) cells by fluorescence imaging after excitement at 488 nm. Au NCs ($HAuCl_4$, 30 μM), Au-miR-34a NCs (miR-34a, 100 nM; $HAuCl_4$, 30 μM), Au-miR-200a NCs (miR-200a, 50 nM; $HAuCl_4$, 30 μM) and Au-let-7a NCs (let-7a, 100 nM; $HAuCl_4$, 30 μM) groups in SMMC-7721 and L02 cells. Au NCs ($HAuCl_4$, 5 μM) and Au-miRNA NCs (miR-34a/miR-200a/let-7a, 50 nM; $HAuCl_4$, 5 μM) groups in HepG2 cells. (b-d) TEM images of Au-miRNA NCs in cellular extracts from SMMC-7721 cells treated with gold salt and miR-34a, gold salt and miR-200a or gold salt and let-7a, respectively. (e) AFM images of Au-miRNA NCs extracted from SMMC-7721 cells after culture with $HAuCl_4$ and miR-34a for 24 h. (f) The same Au-miRNA NCs after digestion by RNase A for 30 min, and (g) amplification and scribe height analysis of the region of interest in f.

with a maximum absorption peak at approximately 260 nm [39]. Herein, the relevant UV–Vis shows a significant absorption peak at 250-300 nm (Fig. 3a). The UV peak absorbance was significantly higher for the self-assembled Au-miRNA NCs group than for the other groups, and it exhibited a slight red shift, further demonstrating an increase in intracellular miRNA concentration. However, no obvious UV–visible absorption peak was observed at approximately 520 nm, and the Au NCs seldom had the surface plasmon resonance effect of ordinary gold nanoparticles [18]. Moreover, the binding of gold and miRNA did not reach saturation at this time, and the miRNA mimic concentrations were excessive. According to the relevant literatures [40], we found that there was a clear emission peak at 670-680 nm in

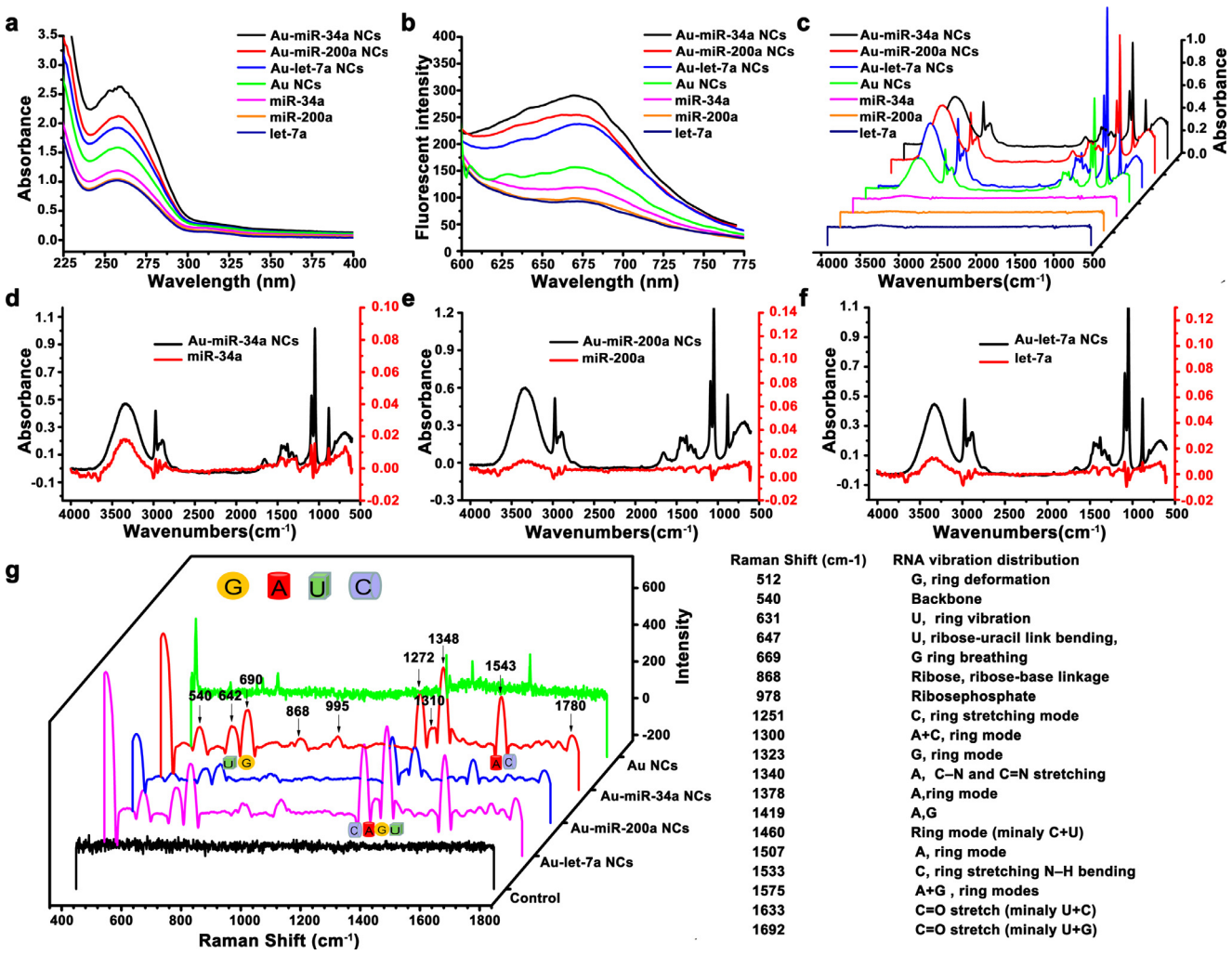


**Fig. 3.** Optical properties of *in situ* biosynthesized Au-miRNA NCs. (a) UV–Vis absorption spectra of Au-miRNA NCs, Au NCs and control groups. (b) Fluorescence emission spectra of Au-miRNA NCs, Au NCs and control groups (excited at 570 nm). (c) FTIR spectra: 3D displays of Au-miRNA NCs, Au NCs and control group. (d–f) Sub-FTIR spectroscopy illustration of miR-34a, miR-200a and let-7a. (g) SERS analysis of the Au-miRNA NCs group compared to the control and Au NCs group. The controls were only miRNA, without the addition of gold salt. Each sample was repeated three times. A, adenine; C, cytosine; G, guanine; U, uracil.

the presence of Au-miRNA NCs under an excitation wavelength of 570 nm, which was significantly different compared to that of the other groups (Fig. 3b). The combination of Au-miRNA NCs resulted in a distinct emission peak at 670-680 nm. This also serves as direct evidence for Au-miRNA NCs fluorescence imaging and the interactions between miRNA and gold. Fluorescence properties can vary considerably depending on the nature of the metal ion interaction. Although the emission spectra of miR-34a, miR-200a, and let-7a are all approximately around 670-680 nm, the emission curves are not completely consistent due to differences in the ion size and linkage of Au-miRNA NCs. It is worth mentioning that the near-infrared fluorescent Au-miRNA NCs have excellent *in vivo* penetration ability and could thus be readily used for *in vivo* fluorescence labeling; this also lays a foundation for Au-miRNA NCs use for *in vivo* fluorescence imaging.

The Fourier transform infrared (FTIR) spectroscopic results showed significant changes in the self-assembled Au-miRNA NCs group compared with the other groups (Fig. 3c). The main change fingerprint peak was 3400–3250 $cm^{-1}$ (N–H stretch amino or ammonia-containing compound), 3000-2800 $cm^{-1}$(C–H stretch), 1500-1600 $cm^{-1}$ (benzene ring skeleton vibration peak), 1650–1580 $cm^{-1}$ (N–H bend), 1250–both 1020 $cm^{-1}$ (C–N stretch) and 910–665 $cm^{-1}$ (N–H wag) had significant changes in the intensity and even had slight displacement (Fig. 3d–f) [41]. Furthermore, the Au-miRNA NCs had distinct surface enhanced Raman spectroscopy (SERS) results compared with the control group (*i.e.*, only miRNA but without gold salt added as a control) and Au NCs group. The specific analyses are shown in Fig. 3g [42,43]. The laser confocal images of cell extracts are also consistent with the nanocluster image of cultured media (Fig. S4). When excited at 488 nm, the fluorescence of the Au-miRNA NCs group was stronger than that of the corresponding extracts from the Au NCs group, while the extracts from L02 cells did not show any fluorescence. Taken together, these fingerprint peaks and features provide clear evidence for the presence of self-assembled Au-miRNA NCs.

### 3.2. In situ *self-assembled Au-miRNA NCs inhibit tumor cells*

We performed toxicity tests on L02, HepG2 and SMMC-7721 cells. It shows that $HAuCl_4$ has excellent biocompatibility with SMMC-7721, HepG2 and L02 cells. Cell vitality remained greater than 80% after incubation with $HAuCl_4$ for 48 h at a final concentration of $<30$ μM for SMMC-7721 cells and $<5$ μM for HepG2 cells (Fig. 4a). Next, the concentrations of miR-34a, miR-200a, and let-7a for the preparation of Au-miRNA NCs were optimized. The data show that miR-34a, miR-200a, and let-7a had the most obvious inhibitory effect on cellular proliferation at medium concentrations (50–100 nM) (Fig. 4b), and the inhibition effect at 48 h was significantly higher than that at 24 h. We notice that higher doses of miRNAs (200, 500, 1000 nM) failed to improve the cell-killing activity further, the reason behind this may be related to the

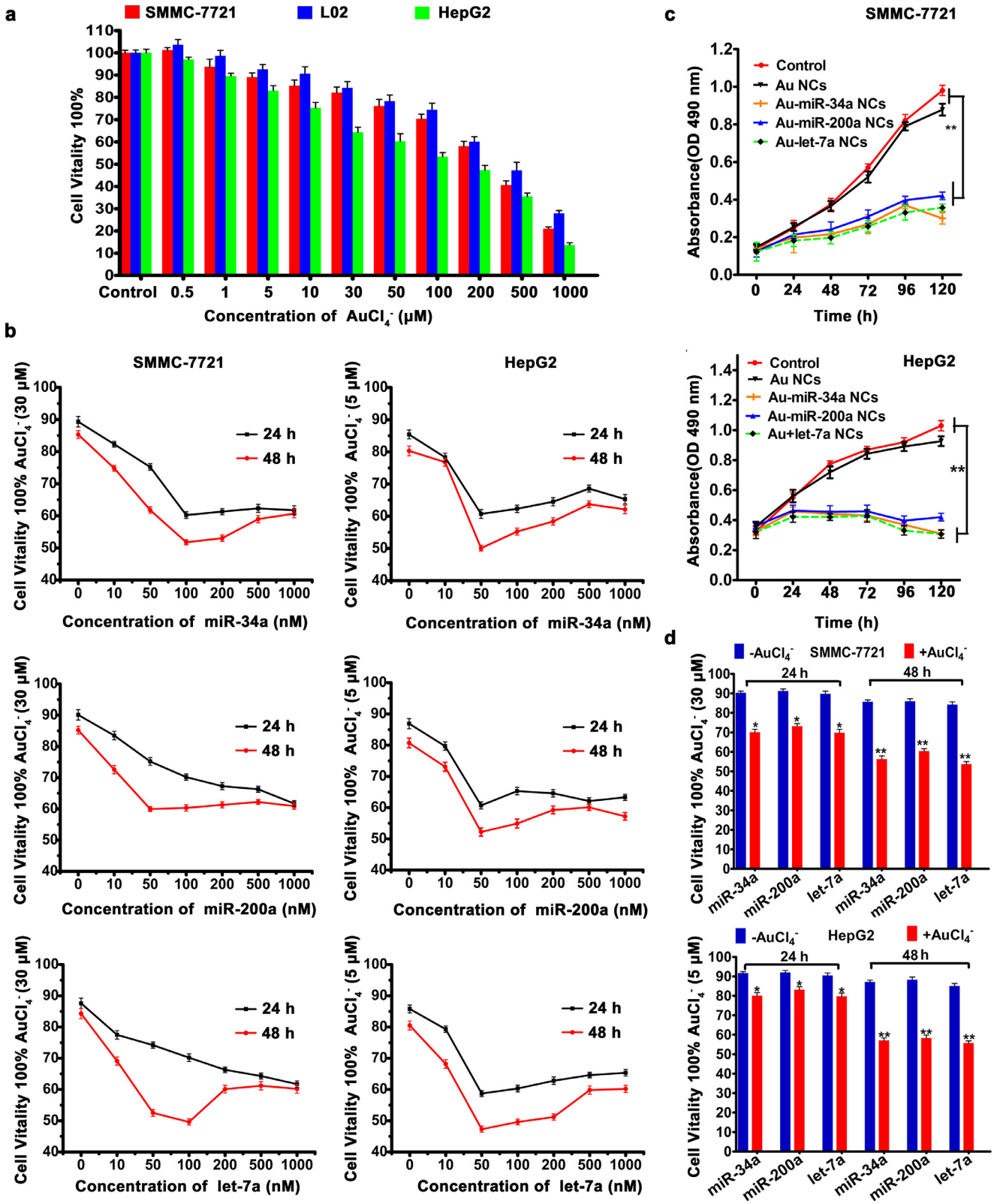


**Fig. 4.** Biochemical characteristics of *in situ* biosynthesized Au-miRNA NCs. (a) MTT analysis of L02, HepG2 and SMMC-7721 cells in the presence of gold salt (error bars: mean ± SD). (b) MTT analysis of HepG2 and SMMC-7721 cells in the presence of Au-miRNA NCs with different concentrations of miR-34a, miR-200a and let-7a (normalized to unprocessed, error bars: mean ± SD). (c) Long-term (5-day) MTT inhibition assay of Au-miRNA NCs in SMMC-7721 (top) and HepG2 (bottom) cells (ANOVA, $^{**}P < 0.01$). (d) miRNA inhibitory effects by miRNAs with (red) and without (blue) gold salt in SMMC-7721 (top) and HepG2 (bottom) cells at 24 h or 48 h. All data were obtained from three separate experiments (*t* test, $^{*}P < 0.05$, $^{**}P < 0.01$).

concentration of Au (III) salt reduction in the tumor microenvironment and the ratio of miRNA mimic. In this study, the concentration of $HAuCl_4$ added was definite, so it is possible that the amount of the reduced Au NCs in relevant complexes can saturate miRNAs at 50-100 nM. In the 5-day MTT inhibition experiments, the proliferation of cells treated with Au-miRNA NCs templated with miR-34a, miR-200a, and let-7a was significantly lower than that of cells in the untreated group and Au NCs group (Fig. 4c). Because naked miRNA may not be internalized by cells, it

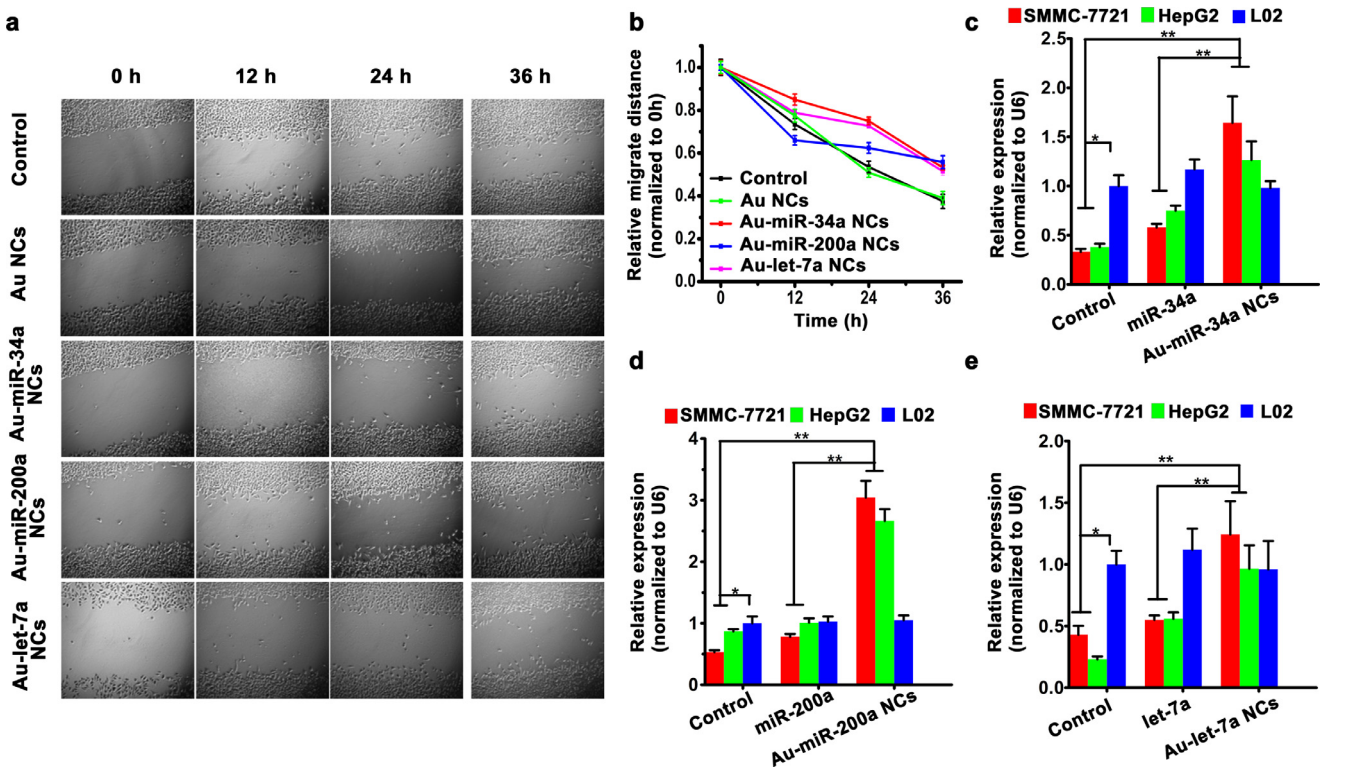


**Fig. 5.** (a and b) The corresponding SMMC-7721 cell scratch wound morphological images (left) and analysis (right) are also displayed. miRNA and gold salt were absent in the control groups under the same conditions. (c) miR-34a, (d) miR-200a and (e) let-7a levels in each group by qRT-PCR analysis (error bars: mean ± SD). All controls were untreated cells (without miRNA or gold salt). qRT-PCR detection control as basal levels. All data were obtained from three separate experiments (*t* test, $^{*}P < 0.05$, $^{**}P < 0.01$).

has to be delivered into cells to induce gene therapeutic effects via carriers. For the *in situ* gold nanotransfection miRNA inhibition analysis, the effect of $HAuCl_4$ solution was significantly higher than that without $HAuCl_4$ solution, with a *P*-value <0.05 at 24 h and <0.01 at 48 h (Fig. 4d). Clear evidence is given by our study that Au-miRNA NCs are beneficial in inhibiting tumor cell growth.

A cell scratch wound assay was used to determine the *in situ* biosynthesis ability of Au-miRNA NCs to inhibit tumor cell invasion and metastasis. From Fig. 5a and b and Fig. S5, it is evident that the addition of $HAuCl_4$ and miR-34a, miR-200a and let-7a significantly inhibited cell proliferation and migration compared to the basal levels and Au NCs conditions. There was no significant difference between the only miRNA group (with no gold salt) and the control group. Additionally, qRT-PCR was used to verify the transfection efficiency of miR-34a, miR-200a, and let-7a (Fig. 5c–e). The results revealed a significant increase in the expression of miRNA in the Au-miRNA NCs -treated groups, which was greater than that of the gold salt-free (only miRNA addition) groups and the control group ($P < 0.05$). However, in L02 cells, there was no significant difference between the Au-miRNA NCs group and the control group.

### 3.3. Interaction between let-7a and gold salt in SMMC-7721 cells

We next aimed to learn more about the targeting mechanism of the Au-miRNA NCs. Let-7 family have been referred to as tumor suppressors [44,45], especially let-7a has strong impact on the the cell cycle of tumor cells [6,46]. Herein, we selected let-7a as an example to investigate how *in situ* self-assembled Au-miRNA NCs can inhibit tumor cell growth. Based on mirror-loaded cell culture microcavity, long-term culture of tumor cells (*i.e.*, SMMC-7721) was carried out to trace the temporospatial processes of cell division blockade and cell death by Au-let-7a NCs (Fig. 6a). During this study, SMMC-7721 cells were incubated with let-7a and $HAuCl_4$ solution for 6 h and then transferred to a mirror-loaded cell culture microcavity. In the 6-h follow-up, the cell cycle of adherent SMMC-7721 cells was arrested, and the division was delayed due to let-7a transfection. The observed cells had visible grooves at 2 h but failed to differentiate into two daughter cells in subsequent observations. At 5 h, the cell cytoplasm condensed, and the cells shrank. At 6 h, the nuclear envelope ruptured, and the cytoskeleton disintegrated due to apoptosis. It is worth mentioning that as the cells gradually become apoptotic, the fluorescent signals gradually decrease. It may be that let-7a continuously binds to its target gene, and the dissociated Au-miRNA NCs are discharged by the efflux pump [38,47]. Finally, at 6 h, only a small amount of fluorescent substance remained after the Au-miRNA NCs were discharged again due to cell membrane rupture. Under the same conditions, the observation of cells in control and Au NCs groups clearly showed the formation of daughter cells at the end of 6 h.

A large amount of data indicates that the overexpression of let-7a can downregulate the expression of certain oncogenes, such as the transcription factor c-myc, suggesting a mutual regulatory relationship between let-7a and c-myc [48]. We obtained the binding site of let-7a and myc from the TargetScan Human 7.1 database (Fig. S6a) and then screened the top 20 validated target genes of let-7a from the TarBase v.8 database; the results included myc (Fig. S6b). In addition, a dual luciferase assay also verified the binding of let-7a to c-myc (Fig. S6c). To learn more about the targeting mechanism for Au-miRNA NCs, we determined the c-myc level in the let-7a group. In the Au-let-7a NCs group, the c-myc protein (Fig. 6b), and mRNA (Fig. 6c) levels significantly decreased compared with those of the control group. These results provide the basis for miRNA transfection by self-assembled Au NCs and the corresponding antitumor efficiency.

The combination of PTT and gene therapy was accomplished by adding gold salt and let-7a to SMMC-7721 cells for 12 h. After laser irradiation at 640 nm for 8 min, the apoptotic rates were detected by flow cytometry using Annexin V-FITC and PI double staining techniques. Annexin-V is a $Ca^{2+}$-dependent phospholipid-binding protein that is used mainly to detect early apoptosis. PI is a nucleic acid dye that passes through the necrotic cell membrane to stain the nucleus during late

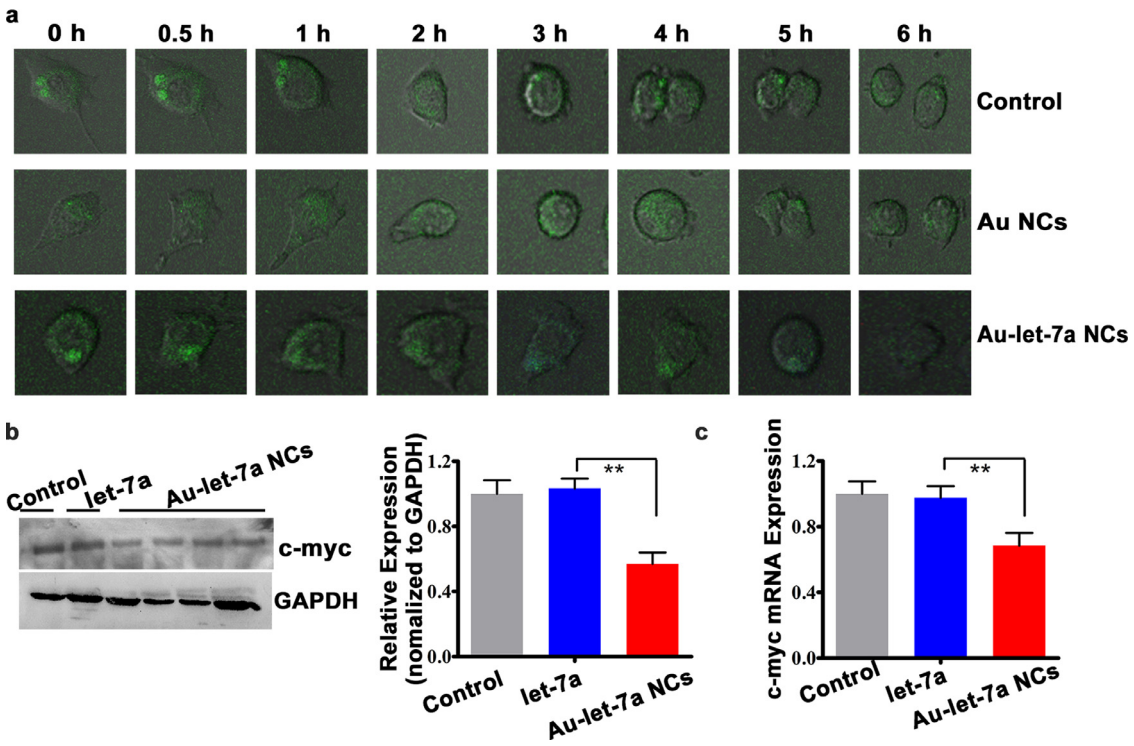


**Fig. 6.** (a) Construction of mirror-loaded cell culture microcavities to trace the temporospatial killing of cancer cells by Au-let-7a NCs in SMMC-7721 cells. Under the same conditions, the observation of cells in the Au-let-7a NCs group tended to apoptosis and failed to differentiate into two daughter cells, but the cells in control and Au NCs groups clearly showed the formation of daughter cells at the end of 6 h. miRNA and gold salt were absent in the control groups under the same conditions. Photographed using a confocal microscope, with 488 nm excitation. (b) Western blot of c-myc protein levels after incubation with gold salt and let-7a in SMMC-7721 cells. (c) qRT-PCR assay of c-myc mRNA levels after incubation with gold salt and let-7a in SMMC-7721 cells. In b and c, the control group contains only let-7a, without gold salt (error bars: mean ± SD; *t* test, $^{**}P < 0.01$). All data were obtained from three separate experiments. In the above assays, the concentrations of let-7a were 100 nM, and the concentration of the gold salt was 30 μM.

apoptosis. The results demonstrated that the combination of PTT and gene therapy induced a significant increase in necrosis and apoptosis in SMMC-7721 cells (Fig. S7). It is thus evident that self-assembled Au-miRNA NCs can be transferred to tumor tissue during PTT. At the same time, biological systems usually increase thermal conductivity and generate heat to dissipate into the surrounding environment, forming a favorable photothermal treatment platform for killing cancer cells. The combination of self-assembled Au-miRNA NCs with PTT proved to induce a higher apoptotic rate than single therapy, which may reveal that Au-let-7a NCs not only play a role in Au-miRNA NCs hyperthermia but also effectively deliver let-7a to target cells and induce apoptosis in SMMC-7721 cells.

### 3.4. Au-let-7a NCs for tumor imaging and inhibition in mice

Based on the above observations, we further performed an *in vivo* study with nude mice (Fig. S8). First, we explore whether *in situ* self-assembled Au-miRNA NCs can be effectively delivered to tumors by using real-time *in vivo* fluorescence imaging. We used the let-7a mimic for the *in vivo* delivery for the bioimaging study. As illustrated in Fig. 7a, the relevant schematic diagram shows the primary tumor imaging procedure in the experimental design. Briefly, xenograft tumor inoculation was performed by injecting HepG2 cells, and the HCC tumor model was successfully constructed. Tumor-bearing mice were divided into four groups (*i.e.*, PBS, Au NCs, let-7a and biosynthesized Au-let-7a NCs, n = 4–5). Subcutaneous injections were performed near the tumor according to the grouping requirements, and fluorescence imaging was performed at 0 h, 2 h, 12 h, 24 h, and 48 h (Fig. 7b and Fig. S9a). Through *in vivo* experimental studies, it was evident that the *in situ* biosynthesis of Au-let-7a NCs enables rapid and accurate targeted imaging of tumors within 2 h after injection (Fig. S9b). The average intensity of this fluorescent signal gradually increased over time until the intensity reached a maximum at 24 h. At 48 h, the average intensity of the relevant fluorescent signal decreased. Compared with the biosynthesized gold nanoclusters alone, the *in situ* self-assembled Au-let-7a NCs can specifically target tumor tissues for efficient bioimaging and drug delivery, accompanied by an apparent red shift in fluorescence emission wavelengths (Fig. 7c). This is consistent with the *in vitro* fluorescence studies described above. It also demonstrates the presence of *in situ* self-assembled Au-miRNA-NCs and enables *in vivo* bioimaging and effective tumor treatment.

To explore the therapeutic effect on tumors, we injected gold salt and let-7a subcutaneously into model mice bearing HepG2 xenograft tumors, with one injection every 3 days for six cycles (Fig. 7a). The control groups included treatment with PBS, only let-7a or only gold salt. The tumor volume dramatically reduced in the groups treated with *in situ* self-assembled Au-let-7a NCs, but this reduction was not observed in the other groups (Fig. 7d). On day 18, we euthanized all mice and harvested the tumor xenografts for further analyses. *Ex vivo* evaluation of the excised organs (Fig. 7e) shows that the *in situ* self-assembled Au-let-7a NCs predominantly accumulated in the tumor site, while almost no or little fluorescence was observed in the other organs (Fig. S9d). *Ex vivo* evaluation of the excised organs in the groups treated with only gold salt also demonstrated that the fluorescence was located in the tumors and liver (Fig. S9c). Note that the biosynthesized Au NCs in the group treated with only gold salt were eventually excreted by the liver, while the *in situ* self-assembled Au-let-7a NCs exerted a biological effect in the tumor cells and were eventually excreted in other forms, with no fluorescence detected in the liver or other organs. Moreover, *in situ* self-assembled Au-let-7a NCs effectively inhibited tumor growth (Fig. 7f). It is evident that the biosynthesized Au-let-7a NCs strongly reduced the tumor burden (by > 50%) compared with treatment with only let-7a, only gold salt or PBS (Fig. 7g). In addition, partial necrosis and nuclear pyknosis were observed in the Au-let-7a NCs group after treatment according to H&E-stained tissue sections (Fig. S11). This further proves that *in situ* self-assembled Au-let-7a NCs have therapeutic efficacy against tumors.

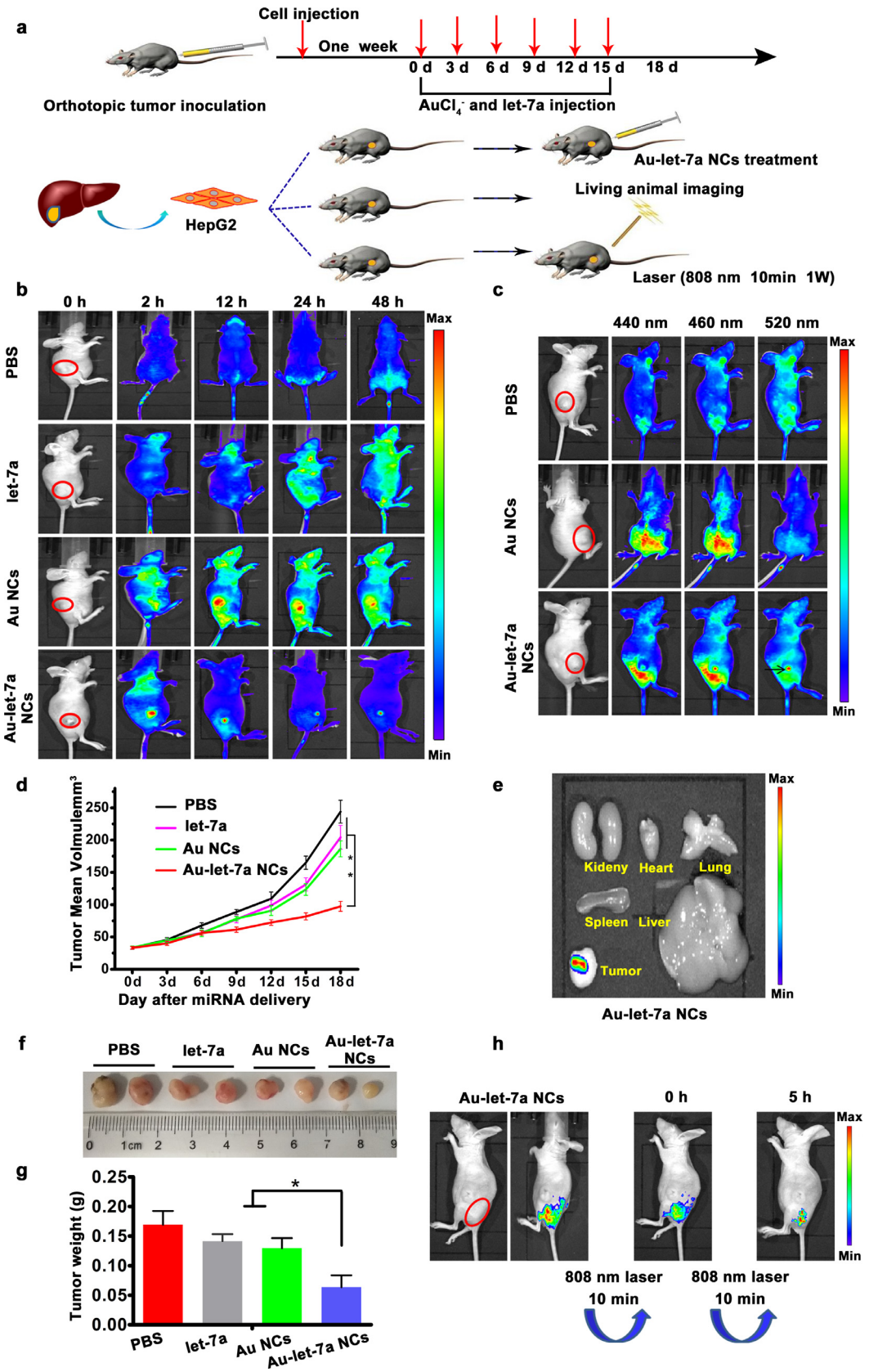


**Fig. 7.** Systematic delivery of Au-let-7a NCs inhibits tumor growth in mice. (a) Schematic diagram illustrating the nude mouse experimental design and primary tumor imaging. (b) *In vivo* fluorescent images after subcutaneous injection of HepG2 cells in different treatment groups at 0 h, 2 h, 12 h, 24 h and 48 h (excitation wavelength: 460 nm). (c) *In vivo* fluorescence imaging of tumor-bearing mice at different excitation wavelengths. (d) Time course of HepG2 tumor growth after different treatments (n = 4–5 mice per group). Tumor sizes were measured every 3 days (ANOVA, $^{**}P < 0.01$). (e) Representative images of dissected organs from a HepG2 tumor-bearing mouse from the Au-let-7a NCs group. (f) Photos of HepG2 tumor xenografts in mice from different treatment groups sacrificed on day 18 after injection. (g) Tumor weights in each group on day 18 (n = 4–5, error bars: mean ± SD; *t* test, $^{*}P < 0.05$). (h) *In vivo* fluorescence monitoring of tumor ablation in mice by near-infrared PTT 12 h after injection of Au-let-7a NCs (n = 3). Tumors were measured with a Vernier caliper, and tumor volume was calculated as follows: volume ($mm^3$) = width × (length$^2$) × 1/2. The red arrows represent the treatment times (subcutaneous injection).

Furthermore, we observed that the apparent therapeutic effect on tumors could be achieved in a short time when near-infrared PTT treatment was performed 12 h after subcutaneous injection of gold salt and let-7a into tumor-bearing mice (Fig. S10b). According to fluorescence imaging, the fluorescence of *in situ* self-assembled Au-let-7a NCs significantly decreased after two laser irradiation (808 nm) sessions for 10 min (Fig. 7h and Fig. S10c), while for Au NCs, little change was observed under the same experimental conditions (Fig. S10a bottom panel and S10c). The combination of PTT and gene therapy with *in situ* self-assembled Au-let-7a NCs can effectively inhibit the growth of tumors in a short time. To monitor the safety of Au-miRNA NCs, the mouse body weights were measured. During the 18-day treatment, no significant changes in body weight were observed among the four groups (Fig. S9e). In addition, treatment at the Au-let-7a NCs dosage and frequency used in our study showed almost no or little toxic effect on the overall health of the tested animals (Fig. S12). These results indicated that *in situ* self-assembled Au-let-7a NCs have therapeutic efficacy against tumors without apparent toxicity or side effects.

## 4. Discussion

As a type of fluorescent nanomaterial, precious metal nanoclusters have the advantages of ultra-small particle size, unique physical and chemical properties, and excellent biocompatibility; thus, they serve as great probes for the early diagnosis of diseases such as tumors. These nanoclusters have received considerable attention in the field of biomedicine. miRNA-based gene therapy has made significant progress; specifically, miRNA mimics (functionally similar to endogenous miRNAs) are employed to reprogram cancer cells by incorporation into RNA-induced silencing complexes. However, the delivery of miRNAs is limited by many barriers, such as low cellular uptake, immunogenicity, renal clearance, degradation by nucleases, elimination by phagocytic immune cells, poor endosomal release, and untoward side effects due to high dose therapy [38,49]. Considering these barriers, there are many reports that use probes [50] and adenovol- and lentiviral-based delivery carriers for miRNAs for transfection [51]. Even though miRNA targeting has been greatly improved, biological toxicity and side effects are also inevitable. Nonviral-based vectors are challenged by their unsatisfactory efficiency, toxicity, and lack of specificity [52]; therefore, our study presents a new strategy for using *in situ* self-assembled Au-miRNA NCs for miRNA delivery and treatment, which has significant advantages in precise tumor bioimaging and drug delivery systems, including high biocompatibility and targeting efficiency. This raises the possibility of providing a new idea for miRNA-based tumor therapy.

In summary, in this study, bright intracellular fluorescence from *in situ* self-assembled fluorescent Au-miRNA NCs was observed in tumor cells after miRNA and $HAuCl_4$ solution coculture. TEM and AFM characterization demonstrated various conformational states of the *in situ* self-assembled fluorescent Au-miRNA NCs. In addition, SERS and FTIR spectra provided characteristic fingerprint peaks of the related miRNA, and remarkable changes in UV−vis absorption and fluorescence spectra support the presence of intracellular Au-miRNA NCs. Our observations demonstrate the effect of the *in situ* self-assembled Au-miRNA NC transfection of miRNA from a biological perspective by cell scratch wound, qRT-RCR, and Western blot assays. These results provide a solid theoretical basis for the targeting and safety of miRNA-based tumor therapy. Owing to the microenvironment of cancer cells, the *in situ* self-assembled Au-miRNA NCs were found exclusively in tumor cells, and not in normal cells such as L02 cells. Moreover, the *in vivo* nude mouse study demonstrated that this self-assembly of Au-let-7a NCs not only allows rapid and specific targeting of tumor tissues but also enables efficient bioimaging and tumor growth inhibition. It is also important that self-assembled Au-miRNA NCs gene therapy combined with PTT can be used for liver cancer cell treatments. The new strategy of *in situ* self-assembled fluorescent Au-miRNA NCs could be used to precisely target cancer cells/tissues for accurate bioimaging and therapy, which may provide fresh insight into the understanding and efficient treatment of cancers such as hepatic carcinoma.

## Declaration of Competing Interest

The authors declare no competing financial interests.

## Funding sources

This work was supported by the National Natural Science Foundation of China (91753106), the Primary Research & Development Plan of Jiangsu Province (BE2019716) and the National Key Research and Development Program of China (2017YFA0205300). The funders had no role in the study design, data collection, data analysis, data interpretation, and writing of the report.

## Supplementary materials

Supplementary material associated with this article can be found in the online version at doi:10.1016/j.ebiom.2020.102740.

## References

[1] Labatut AE, Mattheolabakis G. Non-viral based miR delivery and recent developments. Eur J Pharm Biopharm 2018;128:82–90.
[2] Rupaimoole R, Slack FJ. MicroRNA therapeutics: towards a new era for the management of cancer and other diseases. Nat Rev Drug Discov 2017;16(3):203–22.
[3] Moles R. MicroRNAs-based therapy: a novel and promising strategy for cancer treatment. Microrna 2017;6(2):102–9.
[4] Wang V, Wu W. MicroRNA-based therapeutics for cancer. BioDrugs 2009;23(1):15–23.
[5] Wang Z. The guideline of the design and validation of MiRNA mimics. Methods Mol Biol 2011;676:211–23.
[6] Wang QZ, Lv YH, Gong YH, Li ZF, Xu W, Diao Y, et al. Double-stranded Let-7 mimics, potential candidates for cancer gene therapy. J Physiol Biochem 2012;68(1):107–19.
[7] Melo SA, Kalluri R. Molecular pathways: MicroRNAs as cancer therapeutics. Clin Cancer Res 2012;18(16):4234–9.
[8] Xin Y, Huang M, Guo WW, Huang Q, Zhang LZ, Jiang G. Nano-based delivery of RNAi in cancer therapy. Mol Cancer 2017;16(1):134.
[9] Jin B, Wang W, Meng XX, Du G, Li J, Zhang SZ, et al. Let-7 inhibits self-renewal of hepatocellular cancer stem-like cells through regulating the epithelial-mesenchymal transition and the Wnt signaling pathway. BMC Cancer 2016;16(1):863.
[10] van Rooij E, Kauppinen S. Development of microRNA therapeutics is coming of age. EMBO Mol Med 2014;6(7):851–64.
[11] Takahashi K, Yan I, Wen HJ, Patel T. microRNAs in liver disease: from diagnostics to therapeutics. Clin Biochem 2013;46(10-11):946–52.
[12] Stylianopoulos T, Jain RK. Combining two strategies to improve perfusion and drug delivery in solid tumors. Proc Natl Acad Sci USA 2013;110(46):18632–7.
[13] Heldin CH, Rubin K, Pietras K, Ostman A. High interstitial fluid pressure—an obstacle in cancer therapy. Nat Rev Cancer 2004;4(10):806–13.
[14] Mattheolabakis G, Rigas B, Constantinides PP. Constantinides. Nanodelivery strategies in cancer chemotherapy: biological rationale and pharmaceutical perspectives. Nanomedicine (Lond) 2012;7(10):1577–90.
[15] Mathiyazhakan M, Wiraja C, Xu C. A concise review of gold nanoparticles-based photo-responsive liposomes for controlled drug delivery. Nano-Micro Lett 2018;10(1):10.
[16] Guo WJ, Yuan J, Wang E. Oligonucleotide-stabilized Ag nanoclusters as novel fluorescence probes for the highly selective and sensitive detection of the $Hg^{2+}$ion. Chem Commtm 2009;23:3395–7.
[17] Dimonte A, Frache S, Erokhin V, Piccinini G, Demarchi D, Milano F, et al. Nanosized optoelectronic devices based on photoactivated proteins. Biomacromolecules 2012;13(11):3503–9.
[18] Zheng J, Nicovich PR, Dickson RM. Highly fluorescent noble-metal quantum dots. Annu Rev Phys Chem 2007;58:409–31.
[19] Berti L, Burley GA. Nucleic acid and nucleotide-mediated synthesis of inorganic nanoparticles. Nat Nanotechnol 2008;3(2):81–7.
[20] Ritchie CM, Johnsen KR, Kiser JR, Antoku Y, Dickson RM, Petty JT. Ag nanocluster formation using a cytosine oligonucleotide template. J Phys Chem C Nanomater Interfaces 2007;111(1):175–81.
[21] Zhang X, Sun CQ, Hirao H. Guanine binding to gold nanoparticles through nonbonding interactions. Phys Chem Chem Phys 2013;15(44):19284–92.
[22] Zhang K, Kaufman RJ. From endoplasmic-reticulum stress to the inflammatory response. Nature 2008;454(7203):455–62.
[23] Lim CK, Lee YD, Na J, Oh JM, Her S, Kim K, et al. Chemiluminescence- generating nanoreactor formulation for near-infrared imaging of hydrogen peroxide and glucose level in vivo. Adv Funct Mater 2010;20(16):2644–8.

[24] Du TY, Zhao CQ, Rehman FU, Lai LM, Li XQ, Sun Y, et al. In situ multimodality imaging of cancerous cells based on a selective performance of $Fe^{2+}$-adsorbed zeolitic imidazolate framework-8. Adv Funct Mater 2017;27(5):1603926.
[25] Gong BS, Wang R, Xu HX, Miao MY, Yao ZZ. Nanotherapy targeting the tumor microenvironment. Curr Cancer Drug Targets 2019;19(7):525–33.
[26] Zhou Z, Lu ZR. Molecular imaging of the tumor microenvironment. Adv Drug Deliv Rev 2017;113:24–48.
[27] Wu G, Li Z, Wang Y, Ju X, Huang R. miR-34a inhibits cell proliferation by targeting SATB2 in hepatocellular carcinoma. Biomed Res Int 2018;2018:2863902.
[28] Chen SY, Ma DN, Chen QD, Zhang JJ, Tian YR, Wang ZC, et al. MicroRNA-200a inhibits cell growth and metastasis by targeting Foxa2 in hepatocellular carcinoma. J Cancer 2017;8(4):617–25.
[29] Liu YM, Xia Y, Dai W, Han HY, Dong YX, Cai J, et al. Cholesterol-conjugated let-7a mimics: antitumor efficacy on hepatocellular carcinoma in vitro and in a preclinical orthotopic xenograft model of systemic therapy. BMC Cancer 2014;14:889.
[30] Kaur N, Aditya RN, Singh A, Kuo TR. Biomedical applications for gold nanoclusters: recent developments and future perspectives. Nanoscale Res Lett 2018;13(1):302.
[31] Ong ZY, Chen S, Nabavi E, Regoutz A, Payne DJ, Elson DS, et al. Multibranched gold nanoparticles with intrinsic LAT-1 targeting capabilities for selective photothermal therapy of breast cancer. ACS Appl Mater Interfaces 2017;9(45):39259–70.
[32] Wang BK, Yu XF, Wang JH, Li ZB, Li PH, Wang H, et al. Gold-nanorods-siRNA nanoplex for improved photothermal therapy by gene silencing. Biomaterials 2016;78:27–39.
[33] Rehman FU, Du T, Shaikh S, Jiang X, Chen Y, Li X, et al. Nano in nano: Biosynthesized gold and iron nanoclusters cargo neoplastic exosomes for cancer status biomarking. Nanomedicine 2018;14(8):2619–31.
[34] Dou J, Gu N. Emerging strategies for the identification and targeting of cancer stem cells. Tumor Biol 2010;31:243–53.
[35] Wang M, Chen Y, Cai W, Feng H, Du T, Liu W, et al. In situ self-assembling Au-DNA complexes for targeted cancer bioimaging and inhibition. Proc Natl Acad Sci U S A 2020;117(1):308–16.
[36] Gabelica V, Rosu F, Tabarin T, Kinet C, Antoine R, Broyer M, et al. Base-dependent electron photodetachment from negatively charged DNA strands upon 260-nm laser irradiation. J Am Chem Soc 2007;129(15):4706–13.
[37] Wang J, Zhang G, Li Q, Jiang H, Liu C, Amatore C, et al. In vivo self-bio-imaging of tumors through in situ biosynthesized fluorescent gold nanoclusters. Sci Rep 2013;3:1157.
[38] Gandhi NS, Tekade RK, Chougule MB. Nanocarrier mediated delivery of siRNA/miRNA in combination with chemotherapeutic agents for cancer therapy: current progress and advances. J Control Release 2014;194:238–56.
[39] Wells BD, Yang JT. A computer probe of the circular dichroic bands of nucleic acids in the ultraviolet region. II. Double-stranded ribonucleic acid and deoxyribonucleic acid. Biochemistry 1974;13(7):1317–21.
[40] Wang J, Jia Z. Metal nanoparticles/porous silicon microcavity enhanced surface plasmon resonance fluorescence for the detection of DNA. Sensors (Basel) 2018;18(2):661.
[41] Parker FS. Application of infrared spectroscopy in biochemistry biology and medicine. New York: Plenum Press; 1971.
[42] Morla-Folch J, Xie HN, Alvarez-Puebla RA, Guerrini L. Fast optical chemical and structural classification of RNA. ACS Nano 2016;10(2):2834–42.
[43] Hobro AJ, Standley DM, Ahmad S, Smith NI. Deconstructing RNA: optical measurement of composition and structure. Phys Chem Chem Phys 2013;15(31) 13199-8.
[44] Kumar MS, Erkeland SJ, Pester RE, Chen CY, Ebert MS, Sharp PA, et al. Suppression of non-small cell lung tumor development by the let-7 microRNA family. Proc Natl Acad Sci USA 2008;105(10):3903–8.
[45] Chirshev E, Oberg KC, Ioffe YJ, Unternaehrer JJ. Let-7 as biomarker, prognostic indicator, and therapy for precision medicine in cancer. Clin Transl Med 2019;28(1):24. 8.
[46] Schultz J, Lorenz P, Gross G, Ibrahim S, Kunz M. MicroRNA let7b targets important cell cycle molecules in malignant melanoma cells and interferes with anchorage-independent growth. Cell Res 2008;18:549–57.
[47] Tyagi N, Arora S, Deshmukh SK, Singh S, Marimuthu S, Singh AP. Exploiting nanotechnology for the development of microRNA-based cancer therapeutics. J Biomed Nanotechnol 2016;12(1):28–42.
[48] Liu Y, Yin B, Zhang C, Zhou L, Fan J. Hsa-let-7a functions as a tumor suppressor in renal cell carcinoma cell lines by targeting c-myc. Biochem Biophys Res Commun 2012;417(1):371–5.
[49] Xu Dan, Hu Zhenhua, Su Jing, Wu Fei, Yuan Weien. Micro and nanotechnology for intracellular delivery therapy protein. Nano-Micro Lett 2012;4(2):118–23.
[50] Ekin A, Karatas OF, Culha M, Ozen M. Designing a gold nanoparticle-based nanocarrier for microRNA transfection into the prostate and breast cancer cells. J Gene Med 2014;16(11-12):331–5.
[51] K Choi KM, Choi SH, Jeon H, Kim IS, Ahn HJ. Chimeric capsid protein as a nanocarrier for siRNA delivery: stability and cellular uptake of encapsulated siRNA. ACS Nano 2011;5(11):8690–9.
[52] Ledford H. Drug giants turn their backs on RNA interference. Nature 2010;468(7323):487.